



# Structure-controlled SnSe<sub>2</sub> nanosheets as high performance anode material for lithium ion batteries

Yayi Cheng<sup>1,2</sup> · Jianfeng Huang<sup>2</sup> · Liyun Cao<sup>2</sup> · Hui Xie<sup>1</sup> · Yongfeng Wang<sup>1</sup> · Yanlong Wang<sup>1</sup> · Hongqiang Wu<sup>1</sup> · Shaohua Xi<sup>1</sup> · Jiayin Li<sup>2</sup>

Received: 22 July 2019 / Revised: 21 September 2019 / Accepted: 22 October 2019 / Published online: 3 January 2020  
© Springer-Verlag GmbH Germany, part of Springer Nature 2020

## Abstract

SnSe<sub>2</sub> is regarded as one of the promising anode materials for the advanced lithium ion batteries (LIBs) due to its high theoretical capacity and good conductivity. In this work, SnSe<sub>2</sub> with controllable structure is synthesized by a facile solvothermal method and the influence of reductant on the morphology is revealed. It is found that interconnected SnSe<sub>2</sub> nanosheet assembled by ultrafine nanoparticles exhibits excellent electrochemical performance. As LIBs anode material, the SnSe<sub>2</sub> nanosheet delivers a high initial reversible capacity of 932 mAh g<sup>-1</sup> with the coulombic efficiency of 75.2% at 200 mA g<sup>-1</sup>, remaining at 334 mAh g<sup>-1</sup> over 200 cycles. This highly reversible capacity and cycling stability are mainly ascribed to its special interconnected thin nanosheets structure, which could provide a three-dimensional network paths for ultrafast charge transfer.

**Keywords** Tin diselenide · Nanosheet · Lithium-ion battery · Anode materials

## Introduction

Presently, many kinds of new-type secondary rechargeable batteries have been developed to replace primary lithium battery, such as lithium-ion batteries (LIBs) [1–3], sodium-ion batteries (NIBs) [4–6], potassium-ion batteries (KIBs) [7], and Li-air batteries [8]. Among them, LIBs are regarded as primary candidates for portable electronics, smart power grids, and electric vehicles [9, 10] because LIBs exhibit many advantages of high energy density, high power capability, long lifespan, environmental benignity, and so forth [11–13].

Anode, as an important component of LIBs, plays a crucial role in determining the electrochemical performance. While commercial graphite anodes cannot meet the increasing request of the electrodes due to its limited specific capacity (372 mAh g<sup>-1</sup>) and inferior rate capability [14–17]. Therefore, seeking for alternative anode materials with higher theoretical capacity for next-generation LIBs must be put on schedule [18, 19].

Tin-based compounds SnX<sub>2</sub> (X = O, S, Se) with a high theoretical capacity have been investigated as the most promising LIBs anodes to replace graphite. For instance, SnO<sub>2</sub>, SnS<sub>2</sub>, and SnSe<sub>2</sub> deliver theoretical lithium storage capacity of 1494, 645, and 800 mAh g<sup>-1</sup>, respectively [20–23]. Chen et. al reported a rational design of crystalline SnO<sub>2</sub> @ amorphous TiO<sub>2</sub> core-shell nanostructures, having a high reversible capacity of 1259 mAh g<sup>-1</sup> at cycling rate of 80 mA g<sup>-1</sup> [24]. Nevertheless, the high capacity of these SnX<sub>2</sub> materials is yielded at the cost of large volume changes during lithiation/delithiation owing to alloying and conversion reaction as following [25, 26]:

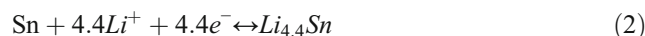
**Electronic supplementary material** The online version of this article (<https://doi.org/10.1007/s11581-019-03321-w>) contains supplementary material, which is available to authorized users.

✉ Jianfeng Huang  
huangjf@sust.edu.cn

✉ Jiayin Li  
lijiajin@sust.edu.cn

<sup>1</sup> School of Materials Engineering, Xi'an Aeronautical University, 259 West Second Ring, Xi'an 710077, China

<sup>2</sup> School of Materials Science & Engineering, Xi'an Key Laboratory of Green Processing for Ceramic materials, Shaanxi Key Laboratory of Green Preparation and Functionalization for Inorganic Materials, Shaanxi University of Science and Technology, Xi'an 710021, China



Among these SnX<sub>2</sub> type anodes, SnSe<sub>2</sub>, as a 2D transition metal chalcogenide material, has attracted much attention as

alternative for graphite anodes [27]. It exhibits special hexagonal layered structures with closely packed sandwich layers, which are stacked by a periodicity of one layer Sn atom and two layers Se atoms, and also the interlayer spaces are loosely bound by van der Waals bonds [28, 29]. To our knowledge, the large interlayer spacing is beneficial for ions intercalations easy and buffering the volume change [23, 29], as reported in  $V_2O_5$  polyhedra anode [7]. However, there are only a handful of reports about  $SnSe_2$  as anodes for LIBs by reason of unsatisfactory electrochemical property. Generally, preparing carbonaceous composite and micro-nanostructure are two effective strategies [30–32], which is beneficial to obtain a high electrical conductivity, large specific surface area, and short  $Li^+$  diffusion routes [2, 33]. For example, Chen et al. reported a two-dimensional  $SnSe_2$ /CNTs hybrid nanostructures that yields a reversible capacity of 210.3 mAh  $g^{-1}$  at 0.1 C after 100 cycles [29]. Huang et al. contributed  $SnSe_2$ /rGO composite that ultra-fine  $SnSe_2$  quantum dots are embedded in a 3D matrix of rGO, which delivers capacities of 778.5 and 324.5 mAh  $g^{-1}$  at current densities of 50 and 5000 mA  $g^{-1}$ , respectively [25]. Zhang et al. reported  $SnSe_2$  2D nanosheets and  $SnSe_2$ /RGO nanocomposites as anode for sodium ions battery, exhibiting a reversible capacity of 515 mAh  $g^{-1}$  after 100 cycles [28].

Herein, we prepared  $SnSe_2$  nanosheets with controllable structure by a simple solvothermal method. The  $SnSe_2$  nanosheets display interconnected three-dimensional networks structure when hydrazine monohydrate is used as a reducing agent. Employed as LIBs anode material, this  $SnSe_2$  material demonstrates excellent cycling stability and rate capability. The detailed reasons are discussed in our work.

## Experimental

### Materials and Chemicals

Stannous chloride dehydrate ( $SnCl_2 \cdot 2H_2O$ , AR, 99.99%), hydrazine monohydrate ( $N_2H_4 \cdot H_2O$ , AR, 85%), ethylenediamine (AR, 80–90%), oleylamine (AR, 80–90%), ethylene glycol (AR, 99.8%), and absolute ethyl alcohol (AR, 75%) were purchased from Sinopharm Chemical Reagent Co., Ltd. Selenium (Se, AR, 99.99%) was obtained from Aladdin Reagent Company. All chemicals were used as received without further purification.

### Materials synthesis

$SnSe_2$  was synthesized by a solvothermal method. In a typical experiment, 0.2256 g  $SnCl_2 \cdot 2H_2O$  was dissolved into 20 mL ethylene glycol to form solution A. Then 0.1579 g Se powder was added into a certain amount of a reducing agent solution (3 mL of hydrazine hydrate and 3 mL of ethylenediamine),

accompanied by magnetic stirring for 1 h to form brick red solution B. After that the solution B was added dropwise into solution A with stirring continuously around 20 min. When oleylamine was used as reductant, 0.2256 g  $SnCl_2 \cdot 2H_2O$  and 0.1579 g Se powder were directly added into 20 mL oleylamine and keep warm at 80–90 °C for 1.5 h. Finally, all mixed solution was separately transferred to 25 mL Teflon-lined stainless-steel autoclave and heated at 180 °C for 12 h at a rotation speed of 10 rpm. The precipitates were filtered and washed with absolute ethanol for six times, and then dried to obtain the final samples. These samples were denoted as S1, S2, and S3 when hydrazine hydrate, ethylenediamine, and oleylamine were adopted as the reducing agent respectively.

### Materials characterization

X-ray diffractometer (XRD) was used to characterize the crystal structure of as-prepared samples, which was recorded on a Rigaku D/max 2200PC V diffractometer operating with Cu  $K\alpha$  radiation ( $\lambda = 1.5406 \text{ \AA}$ ). The morphology and microstructure were investigated by field emission scanning electron microscopy (SEM, S-4800) together with transmission electron microscope (TEM, Tecnai G2F20S-TWIN system).

### Electrochemical tests

For a half-battery, the electrochemical tests of the as-prepared  $SnSe_2$  nanomaterials were performed using CR2032, microporous polypropylene film as the separator, and the Li foil as a reference electrode. The working electrode was prepared by mixing the  $SnSe_2$  nanomaterials (the active materials), sodium carboxymethyl cellulose (CMC) binder, and super p (conductive additives) at a weight ratio of 7:2:1 in water and grounded to form slurry. The slurry was coated on the copper foil and dried in a vacuum oven at 80 °C for 48 h, and then the electrodes were punched into disks with diameter of 15.8 mm. The electrolyte was a solution containing 1 M  $LiPF_6$  dissolved in a mixture of EC (ethylene carbonate), EMC (ethyl methyl carbonate), and DMC (dimethyl carbonate) in volume ratio of 1:1:1. CR2032-type button cell was assembled in an Ar-filled glove box (Mbraun, Germany,  $O_2$  and  $H_2O$  contents < 0.5 ppm). The assembled cells were stood after 48 h to conduct electrochemical tests with the voltage range of 0.001–3.0 V.

## Results and discussion

Figure 1 shows the XRD patterns of tin selenide products, which was prepared by using hydrazine hydrate, ethylenediamine, and oleylamine as a reductant, respectively. All diffraction peaks could be well indexed to hexagonal

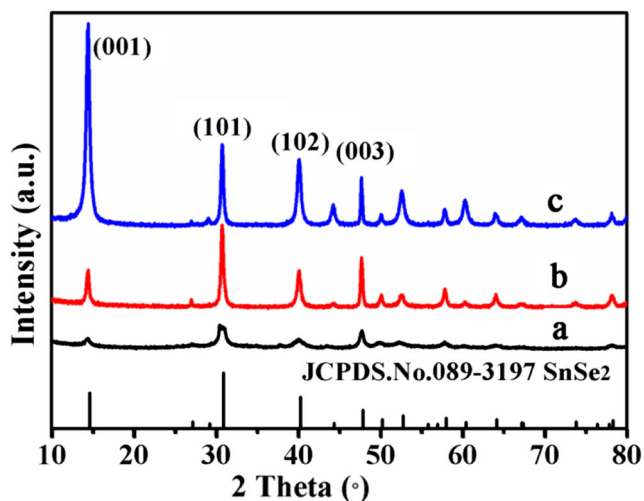


Fig. 1 XRD patterns. a S1 sample. b S2 sample. c S3 sample

SnSe<sub>2</sub> phase with lattice parameters of  $a = 3.8110 \text{ \AA}$ ,  $b = 3.8110 \text{ \AA}$ , and  $c = 6.1410 \text{ \AA}$ . And the prepared SnSe<sub>2</sub> is assigned to the space group P-3 m1(164) according to the JCPDS No. 089-3197. There is no any impurity phase, exhibiting high purity of SnSe<sub>2</sub>. The diffraction peaks centered at 14.4°, 30.7°, 40.04°, and 47.5° are very distinct, corresponding to (001), (101), (102), and (003) crystal facets of SnSe<sub>2</sub>. By comparison, the diffraction peak intensity of products is the lowest when hydrazine hydrate is used as reducing agent, which may be related to the weak crystallinity degree of the SnSe<sub>2</sub> nanocrystals. When ethylenediamine and oleylamine are used as reducing agent, the diffraction peak intensity of the SnSe<sub>2</sub> (001) is much different. Obviously, the intensity of the latter is higher than that of the former. This may be concerned with the orientation of the crystal growth.

SEM was conducted to characterize the morphology of the as-prepared SnSe<sub>2</sub> with using different reductant. As shown in

Fig. 2a and b, the S1 displays uniformly dispersed nanosheet with interconnected structure when hydrazine hydrate as a reductant. The thickness of the nanosheet is less than 20 nm. In Fig. 2c, S2 present stagger flower structure composed by many nanoplate. Further observation from Fig. 2d found that each nanoplate consists of several much thinner nanosheets. When oleylamine is shown in Fig. 2e as a reductant, the S3 demonstrates nanodisk structure with the smallest grain size among three samples. Fig. 2f indicates that the nanodisk is composed of many thinner plates. The phase and microstructure of the SnSe<sub>2</sub> nanocrystals can be further observed by TEM analysis as below.

TEM images of the S1, S2 and S3 samples are shown in Fig. 3. The TEM images of S1 (Fig. 3a) presents nanosheet structure when hydrazine hydrate is adopted as a reductant. In Fig. 3b, S1 shows rough surface, in which many SnSe<sub>2</sub> nanocrystallites with lattice spacing of (101) and (102) planes can be further observed from the lattice resolved HRTEM image in Fig. 3c. And also those nanocrystals exhibit the average particle size of around 5 nm. If SnSe<sub>2</sub> nanosheets are single crystal, then they will present only one crystal planes growing along specific crystal faces. Therefore, we conclude that S1 nanosheets are assembled by many nanoparticles. In Fig. 3d, e, and f, ethylenediamine as a reducing reagent, the corresponding S2 displays nanoplate structure with regular edges, which is self-assembled by many nanoparticles (3–4 nm) similar with the S1 sample. The S3 demonstrates nanodisk structure when oleylamine is employed, shown in Fig. 3g, h, and i. Each nanodisk consists of many ultrafine particles. Further observation from HRTEM image in Fig. 3i, the lattice spacing of SnSe<sub>2</sub> (101), (102), and (003) planes can be detected. All the analysis directly confirms the phase and microstructure of the SnSe<sub>2</sub> nanocrystals prepared by using different reductant, in agreement with the XRD and SEM results.

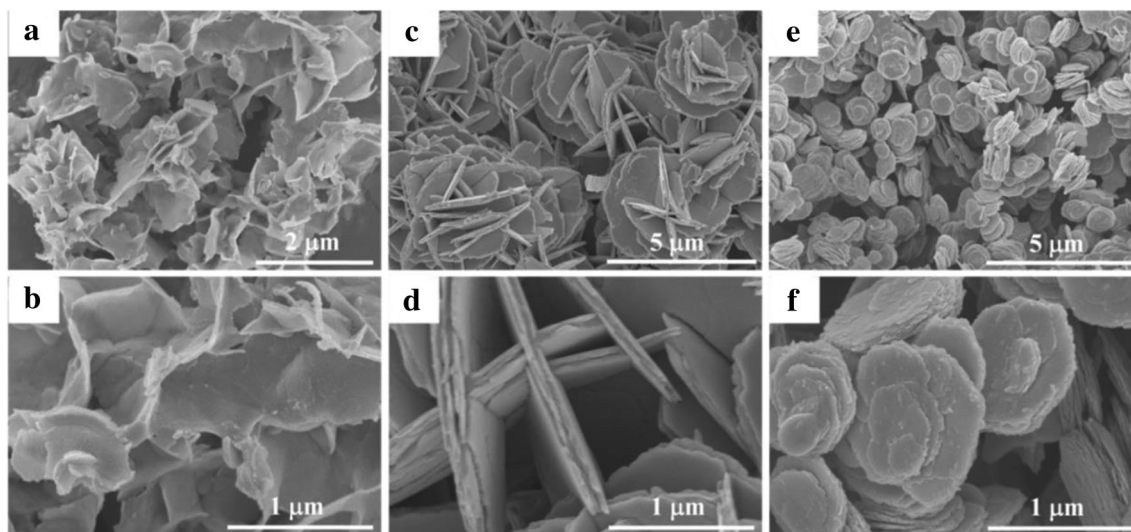
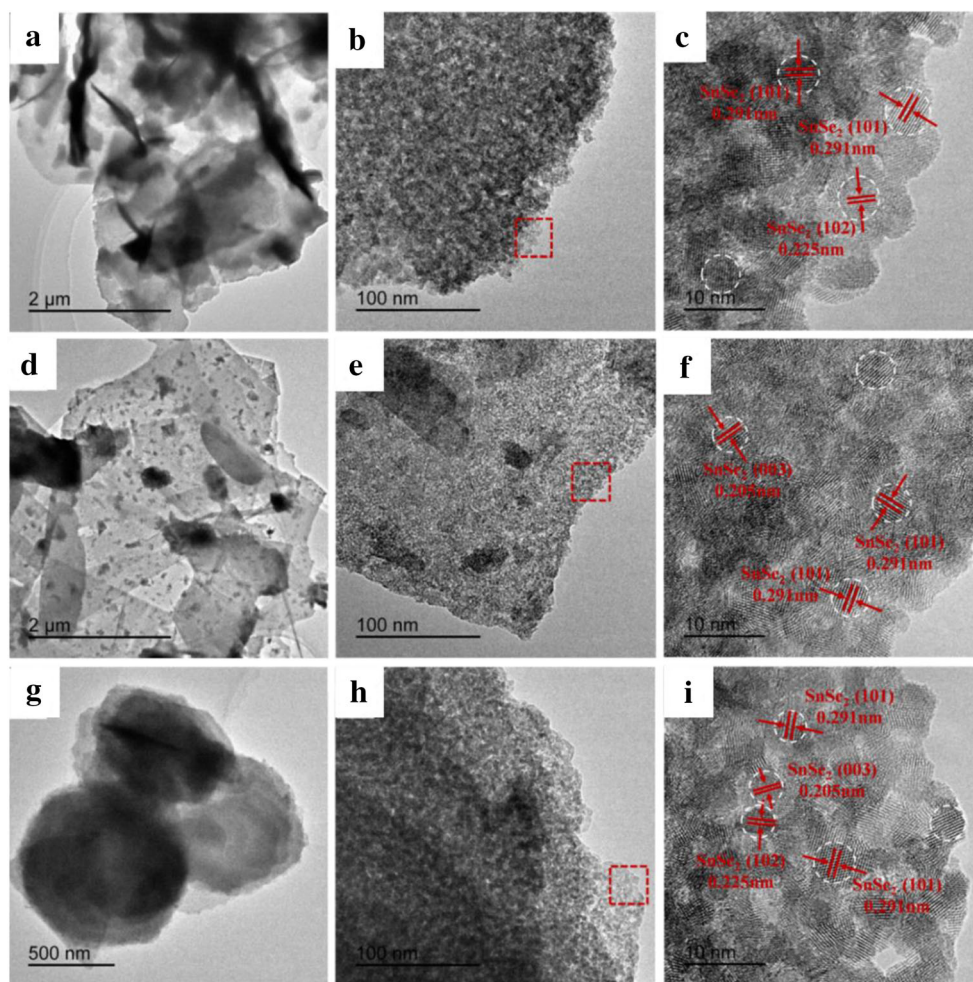


Fig. 2 SEM images. a, b S1 sample. c, d S2 sample. e, f S3 sample



**Fig. 3** TEM and HRTEM images. **a, b, c** S1 sample. **d, e, f** S2. **g, h, i** S3 samples

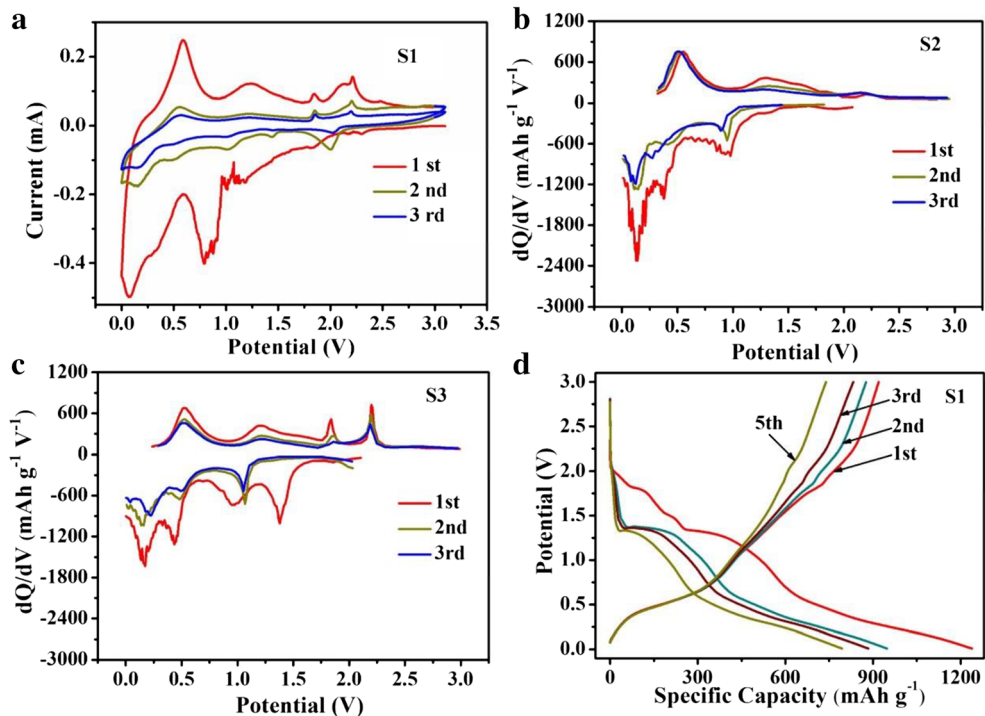


Cyclic voltammetry (CV) curves of S1 electrode was evaluated between 0.001 and 3.0 V at  $0.1 \text{ mV s}^{-1}$  to explore typical electrochemical reaction of the  $\text{SnSe}_2$ . As shown in Fig. 4, two weak reduction peaks could be observed at about 2.35 V and 1.82 V during lithiation process of the initial cycling, corresponding to intercalation reaction of  $\text{SnSe}_2$ . The reduction peaks from 1.23 V to 1.02 V are attributed to the conversion reaction between  $\text{SnSe}_2$  and  $\text{Li}^+$  to form Sn and  $\text{Li}_2\text{Se}$ . More lithium ions react with Sn to form a series of  $\text{Li}_x\text{Sn}$  alloys with the increasing of  $\text{Li}^+$  insertion in the electrode, which are centered at 0.001–0.5 V. It should note that a distinct redox peak at 0.85 V is irreversible, ascribing to formation of the solid-electrolyte interface (SEI) films. In the delithiation process of the 1st cycle, the oxidation peak at  $\sim 0.6$  V is assigned to de-alloying reaction of  $\text{Li}_x\text{Sn}$ . The peaks at  $\sim 1.24$  V, 1.85 V, and 2.21 V are assigned to the conversion reaction from Sn to  $\text{SnSe}_2$  along with the decomposition reaction of  $\text{Li}_2\text{Se}$  [25]. At the 2nd and 3rd cycles, there are five reduction peaks locating at 2.02 V, 1.46 V, 1.04 V, 0.52 V, 0.15 V, and three oxidation peaks at 0.55 V, 1.85 V, and 2.21 V, respectively. These electrochemical reactions are similar to  $\text{SnO}_2$ , which the conversion reaction locates at high voltages and the alloying/de-

alloying reactions at low voltages [34]. In addition, the peak intensity of the 2nd and 3rd cycles is much lower than that of the 1st cycle, illustrating that high irreversible capacity is accompanied with the 1st charge/discharge process. To better compare the electrochemical reaction behavior, the  $dQ/dV$  curves of S2 and S3 electrodes at current density of  $200 \text{ mA g}^{-1}$  were also conducted shown in Fig. 4b and c. It can be seen that S2 and S3 electrodes show similar  $dQ/dV$  curves from 1st to 3rd cycles. They possess nearly same oxidation and reduction peak potential except for peak height. This indicates that  $\text{SnSe}_2$  with different structure show same electrochemical reactions behavior but the different reaction kinetics. In Fig. 4d, the galvanostatic charge/discharge (GCD) profiles of S1 were performed. The GCD profiles of S2 and S3 electrodes were also shown in Figs. S1 and S2. In the initial discharging process, S1 displays three slopes at around 2.0–1.82 V, 1.5–1.0 V, and 0.6–0.001 V, ascribing to intercalation, conversion, and alloying reactions, respectively. There are four slopes in the initial charging process, corresponding to four oxidation peaks in CV curves of S1 electrode.

Cycling performance of S1, S2, and S3 electrodes were compared in Fig. 5a at current density of  $200 \text{ mA g}^{-1}$ . The

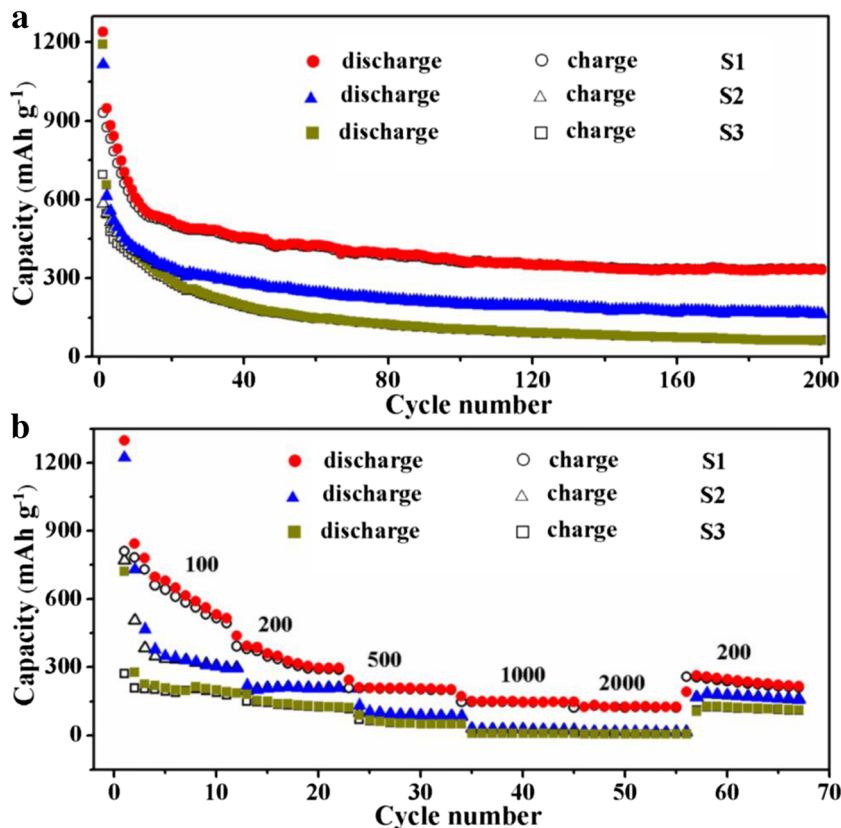
**Fig. 4** **a** Cyclic voltammetry (CV) curves of S1 electrode at a scan rate of  $0.1 \text{ mV s}^{-1}$  in the potential range  $0.001\text{--}3.0 \text{ V}$ . **b** and **c** are  $dQ/dV$  curves of S2 and S3 electrodes at current density of  $200 \text{ mA g}^{-1}$ . **d** Charge-discharge profiles of S1 electrode at  $200 \text{ mA g}^{-1}$



S1, S2, and S3 electrodes deliver initial charging/discharging capacity of  $932/1239 \text{ mAh g}^{-1}$ ,  $583/1114 \text{ mAh g}^{-1}$ , and  $694/1191 \text{ mAh g}^{-1}$ , corresponding to the coulombic efficiency of  $75.2 \%$ ,  $52.3 \%$ , and  $58.2 \%$ , respectively. It indicates that the

initial coulombic efficiency of S1 electrode is much higher in comparison with the S2 and S3 electrodes. In the first 20 cycles, the capacity of all electrodes drops rapidly, and then keeps stable at subsequent 80 cycles. After 200 cycles, the

**Fig. 5** Electrochemical performance of S1, S2, and S3 electrodes. **a** Cycling performance at  $200 \text{ mA g}^{-1}$ . **b** Rate performance at various current density



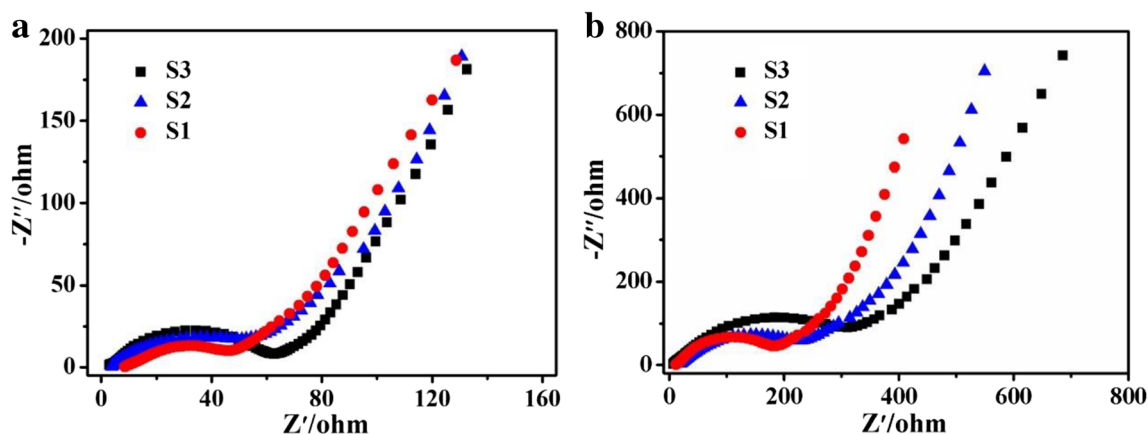


**Fig. 6** Nyquist plots of electrochemical impedance spectroscopy (EIS) for the S1, S2, and S3 electrodes before (a) and after 200 cycles (b)

reversible capacity of the S1, S2, and S3 electrodes maintains 334, 166, and 62 mAh g<sup>-1</sup>, indicating that S1 electrode possesses the best lithium storage performance among the three electrodes. The cycling performance of S1, S2, and S3 electrodes was conducted twice and was shown in Fig. S3. They follow the similar regularity that the cycling property of S1 electrode is the best. Fig. 5b shows the rate capability of the S1, S2, and S3 electrodes at 100, 200, 500, 1000, and 2000 mA g<sup>-1</sup>, which exhibit the reversible capacity of 533/295/191 mAh g<sup>-1</sup>, 298/209/122 mAh g<sup>-1</sup>, 204/86/50 mAh g<sup>-1</sup>, 146/25/20 mAh g<sup>-1</sup>, and 125/15/12 mAh g<sup>-1</sup> at the 10th cycle of the different current density. When the current density is finally reset to 200 mA g<sup>-1</sup>, a reversible capacity of 221 mAh g<sup>-1</sup> could be recovered, which is 1.4 times and 2 times higher than that of S2 (161 mAh g<sup>-1</sup>) and S3 (112 mAh g<sup>-1</sup>) electrodes. By contrast, we can conclude that S1 electrode shows more excellent cycling and rate performance than that of S2 and S3 electrodes.

This superior electrochemical property can be ascribed to the special structure of the S1. The S1 presents thin nanosheets with assembled by many nanoparticles. These nanosheets connect with each other, providing more paths for lithium ions and electrons transfer. In addition, the S1 with low crystallinity can experience an isotropic stress, which has an evidently higher flexibility to avoid its fracture during charge/discharge process than the crystalline one, as reported in other electrode system [24, 35]. The flower structure of S2 is weaved by many nanoplates, and also the nanoplates are stacked by 3~5 layer thin nanosheets, which shall hinder the charge transmission. S3 shows the similar structure with S2 that nanodisk is composed of many thinner plates, making longer time for charge transport. Therefore, the charge rate of S2 and S3 electrodes is slower, exhibiting inferior electrochemical performance.

To make clear the charge transfer behavior of the S1, S2, and S3 electrodes, the electrochemical impedance spectroscopy (EIS) were performed before and after 200 cycling. As shown in Fig. 6, all curves consist of a semicircle at high frequency and an oblique line at low frequency. Generally,

the diameter of the semicircle is related to the charge transfer resistance ( $R_{ct}$ ) and the diagonal line corresponds to the diffusion resistance ( $Z_w$ ) [36, 37]. Before cycling, all the electrodes show the similar semicircle diameter, indicating the close  $R_{ct}$  value. While after 200 cycles, the semicircle diameter of S1 electrode is the minimum, manifesting that the  $R_{ct}$  value of S1 electrode is the lowest compared with S2 and S3 electrodes. Combined with the structure of each electrode, it is demonstrated that interconnected thin nanosheets of S1 provides a three-dimensional networks for charge transfer, facilitating transmission of the lithium ions and electrons in the electrode [38]. S2 and S3 electrodes with stacked structure impede the charge transport, which is disadvantageous to the electrochemical reaction.

## Conclusions

In summary, SnSe<sub>2</sub> with different structure are prepared by adjusting reductant in the solvothermal synthesis process. Various structures with nanosheet, stagger flower, and nanodisk are obtained through using hydrazine monohydrate, ethylenediamine, and oleylamine as a reducing reagent, respectively. In our work, electrochemical studies found that SnSe<sub>2</sub> interconnected nanosheet shows the best electrochemical properties among all the structures. It yields an initial reversible capacity of 932 mAh g<sup>-1</sup> at current density of 200 mA g<sup>-1</sup>, corresponding to the coulombic efficiency of 75.2 %. Even over 200 cycles, a capacity of 334 mAh g<sup>-1</sup> is still remained. The excellent reversible capacity and superiority in cycling stability are attributed to its specific three-dimensional interconnected thin nanosheets structure, facilitating the ultrafast lithium ions and electrons transfer in the electrode. Furthermore, the SnSe<sub>2</sub> nanosheets with low crystallinity can experience an isotropic stress, which has an evidently higher flexibility to avoid its fracture during charge/discharge process. Therefore, we believe this work can



provide new ideas for the design of SnSe<sub>2</sub> microstructure in the application of LIBs anode materials.

**Funding information** This work was financially supported by Scientific Research Program Funded by Shaanxi Provincial Education Department (Program No. 19JK0428), the National Science Foundation of Shaanxi Province (No. 2019JQ-911), the National Natural Science Foundation of China (No. 51672165, 51702198), the Postdoctoral Foundation of China (Special 155660, 2016M592897XB), the National Key Research and Development Program of China (2017YFB0308303-03).

## References

1. Yoon YH, Kim DS, Kim M, Park MS, Lee Y-C, Kim KH, Kim IT, Hur J, Lee SG (2018) Investigation of electrochemical performance on carbon supported tin-selenium bimetallic anodes in lithium-ion batteries. *Electrochim Acta* 266:193–201
2. Zhang L, Lu L, Zhang D, Hu W, Wang N, Xu B, Li Y, Zeng H (2016) Dual-buffered SnSe@CNFs as negative electrode with outstanding lithium storage performance. *Electrochim Acta* 209:423–429
3. Gurung A, Naderi R, Vaagensmith B, Varnekar G, Zhou Z, Elbohy H, Qiao Q (2016) Tin selenide-multi-walled carbon nanotubes hybrid anodes for high performance lithium-ion batteries. *Electrochim Acta* 211:720–725
4. Wang S, Zhang XB (2019) N-doped C@Zn<sub>3</sub>B<sub>2</sub>O<sub>6</sub> as a low cost and environmentally friendly anode material for Na-ion batteries: high performance and new reaction mechanism. *Adv Mater* 31:1–8
5. Wang S, Zhu YH, Yan JM, Zhang XB (2018) P3-type K<sub>0.32</sub>Fe<sub>0.35</sub>Mn<sub>0.65</sub>O<sub>2</sub>·0.39H<sub>2</sub>O: a promising cathode for Na-ion full batteries. *J Mater Chem A* 6:13075–13081
6. Zhao YJ, Wang FX, Wang C, Wang S, Wang CY, Zhao ZW, Duan LL, Liu YP, Wu YP, Li W, Zhao DY (2019) Encapsulating highly crystallized mesoporous Fe<sub>3</sub>O<sub>4</sub> in hollow N-doped carbon nanospheres for high-capacity long-life sodium-ion batteries. *Nano Energy* 56:426–433
7. Zhu YH, Zhang Q, Yang X, Zhao EY, Sun T, Zhang XB, Wang S, Yu XQ, Yan JM, Jiang Q (2019) Reconstructed orthorhombic V<sub>2</sub>O<sub>5</sub> polyhedra for fast ion diffusion in K-ion batteries. *Chemistry* 5: 168–179
8. Ma JL, Meng FL, Yu Y, Liu DP, Yan JM, Zhang Y, Zhang XB, Jiang Q (2018) Prevention of dendrite growth and volume expansion to give high-performance aprotic bimetallic Li-Na alloy-O<sub>2</sub> batteries. *Nat Chem* 11:64–70
9. Li T, Liu B, Liu H, Zou J, Ding Y, Xin T, Wang Y (2019) Copper and carbon co-encapsulated tin dioxide nanocrystals for high performance lithium ion batteries. *J Alloys Compd* 774:565–572
10. Sun T, Li ZJ, Zhang XB (2018) Achieving of high density/utilization of active groups via synergic integration of C=N and C=O bonds for ultra-stable and high-rate lithium-ion batteries. *Research* 1936735:1–10
11. Yang WF, Wang J, Si C, Peng Z, Zhang Z (2017) Tungsten diselenide nanoplates as advanced lithium/sodium ion electrode materials with different storage mechanisms. *Nano Res* 10:2584–2598
12. Xie W, Wang Q, Xu J, Yu Y, Zhao R, Li N, Li M, Du Y, Peng S, Cao G (2019) Microbelt-void-microbelt-structured SnO<sub>2</sub>@C as an advanced electrode with outstanding rate capability and high reversibility. *J Mater Chem A* 7:10523–10533
13. Wu J, Liu J, Wang Z, Gong X, Wang Y (2019) A new design for Si wears double jackets used as a high-performance lithium-ion battery anode. *Chem Eng J* 370:565–572
14. Zhang Z, Zhao X, Li J (2015) SnSe/carbon nanocomposite synthesized by high energy ball milling as an anode material for sodium-ion and lithium-ion batteries. *Electrochim Acta* 176:1296–1301
15. Zhu S, Liu J, Sun J (2019) Precise growth of Al<sub>2</sub>O<sub>3</sub>/SnO<sub>2</sub>/CNTs composites by a two-step atomic layer deposition and their application as an improved anode for lithium ion batteries. *Electrochim Acta* 319:490–498
16. Zhang Z, Xu P, Zhang H, Shen A, Zhao Y (2019) Flexible three-dimensional titanium-dioxide-based hollow nano-flower arrays for advanced lithium-ion battery anodes. *ACS Appl Energy Mater.* <https://doi.org/10.1021/acsaem.9b00869>
17. Xia S, Li F, Shen X, Li X, Cai X, Liu J (2019) Heterostructural SnO/SnO<sub>2</sub>@C composite fabricated from tin-based coordination polymer as high-performance anode materials for lithium ion batteries. *Mater Lett* 251:94–97
18. Wang XM, Wang N, Zhang Q, Shi XF, Yu YN, Chai YJ (2019) Excellent cyclic performance of Fe<sub>2</sub>O<sub>3</sub>@C/SnO<sub>2</sub> controlled by Fe<sub>2</sub>O<sub>3</sub>@C and SnO<sub>2</sub>/C hybrid structures for lithium-ion batteries. *J Phys Chem Solids* 132:130–137
19. Bai J, Wu H, Wang S, Zhang G, Feng C, Liu H (2019) Synthesis of CoSe<sub>2</sub>-SnSe<sub>2</sub> nanocube-coated nitrogen-doped carbon (NC) as anode for lithium and sodium ion batteries. *Appl Surf Sci* 488:512–521
20. Tian Q, Zhang F, Yang L (2019) Fabricating thin two-dimensional hollow tin dioxide/carbon nanocomposite for high-performance lithium-ion battery anode. *Appl Surf Sci* 481:1377–1384
21. Ren L, Yao Y, Wang K, Li S, Zhu K, Liu J (2019) Novel one-step in situ growth of SnO<sub>2</sub> quantum dots on reduced graphene oxide and its application for lithium ion batteries. *J Solid State Chem* 273: 128–131
22. Guan D, Li J, Gao X, Xie Y, Yuan C (2016) Growth characteristics and influencing factors of 3D hierarchical flower-like SnS<sub>2</sub> nanostructures and their superior lithium-ion intercalation performance. *J Alloys Compd* 658:190–197
23. Lee DH, Park CM (2017) Tin selenides with layered crystal structures for Li-ion batteries: interesting phase change mechanisms and outstanding electrochemical behaviors. *ACS Appl Mater Interfaces* 9:15439–15448
24. Chen H, Lu Y, Zhu H, Guo Y, Hu R, Khatoon R, Chen L, Zeng YJ, Jiao L, Leng J, Lu J (2019) Crystalline SnO<sub>2</sub>@amorphous TiO<sub>2</sub> core-shell nanostructures for high-performance lithium ion batteries. *Electrochim Acta* 310:203–212
25. Huang ZX, Liu B, Kong DZ, Wang Y, Yang HY (2018) SnSe<sub>2</sub> Quantum Dot/rGO composite as high performing lithium anode. *Energy Storage Mater* 10:92–101
26. Wei Z, Wang L, Zhuo M, Ni W, Wang H (2018) Layered tin sulfide and selenide anode materials for Li- and Na-ion. *J Mater Chem A* 6: 12185–12214
27. Rena XC, Wang JS, Zhu DM, Li QW, Tian WF, Wang L, Zhang JB, Miao L, Paul KC, Huo KF (2018) Sn-C bonding riveted SnSe nanoplates vertically grown on nitrogen-doped carbon nanobelts for high-performance sodium-ion battery anodes. *Nano Energy* 54:332–330
28. Zhang F, Xia C, Zhu JJ, Ahmed B, Liang HF, Velusamy DB, Schwingschlögl UD, Alshareef HN (2016) SnSe<sub>2</sub> 2D anodes for advanced sodium ion batteries. *Adv Energy Mater* 1601188: 1–10
29. Chen H, Jia BE, Lu X, Guo Y, Hu R, Khatoon R, Jiao L, Leng J, Zhang L, Lu J (2019) Two-dimensional SnSe<sub>2</sub>/CNTs hybrid nanostructures as anode materials for high-performance lithium-ion batteries. *Chem Eur J.* <https://doi.org/10.1002/chem.201901487>
30. Song JS, Cho GB, Kim KW, Ahn HJ, Kim HS, Ahn JH, Cho KK (2019) Fabrication of multilayer graphene-encapsulated Sn/SnO<sub>2</sub>

- nanocomposite as an anode material for lithium-ion batteries and its electrochemical properties. *Appl Surf Sci* 481:736–740
31. Cheng Y, Huang J, Li J, Cao L, Xu Z, Luo X, Qi H, Guo P (2019) SnSe/r-GO composite with enhanced pseudocapacitance as a high-performance anode for li-ion batteries. *ACS Sustain Chem Eng* 7: 8637–8646
  32. Man Q, Hou Q, Liu P, Jin R, Li G (2018) Cube-like  $Sb_2Se_3/C$  constructed by ultrathin nanosheets as anode material for lithium and sodium-ion batteries. *Ionics* 25:1551–1558
  33. Niu F, Yang J, Wang N, Zhang DP, Fan WL, Yang J, Qian YT (2017)  $MoSe_2$ -covered N,P-doped carbon nanosheets as a long-life and high-rate anode material for sodium-ion batteries. *Adv Funct Mater* 1700522:1–11
  34. Cheng Y, Huang J, Qi H, Cao L, Yang J, Xi Q, Luo X, Yanagisawa K, Li J (2017) Adjusting the chemical bonding of  $SnO_2@CNT$  composite for enhanced conversion reaction kinetics. *Small* 1700656:1–11
  35. Fan L, Li X, Yan B, Feng J, Xiong D, Li D, Gu L, Wen Y, Lawes S, Sun X (2016) Controlled  $SnO_2$  crystallinity effectively dominating sodium storage performance. *Adv Energy Mater* 6:1–13
  36. Chen S, Wu Q, Wen M, Wu Q, Li J, Cui Y, Pinna N, Fan Y, Wu T (2018) Sea-sponge-like structure of Nano- $Fe_3O_4$  on skeleton-c with long cycle life under high rate for Li-ion batteries. *ACS Appl Mater Interfaces* 10:19656–19663
  37. Wu X, Li S, Xu Y, Wang B, Liu J, Yu M (2019) Hierarchical heterostructures of NiO nanosheet arrays grown on pine twig-like  $\beta-NiS@Ni_3S_2$  frameworks as free-standing integrated anode for high-performance lithium-ion batteries. *Chem Eng J* 356:245–254
  38. Yuan S, Zhu YH, Li W, Wang S, Xu D, Li L, Zhang Y, Zhang XB (2017) Surfactant-free aqueous synthesis of pure single-crystalline SnSe nanosheet clusters as anode for high energy- and power-density sodium-ion batteries. *Adv Mater* 29:1–6

**Publisher's note** Springer Nature remains neutral with regard to jurisdictional claims in published maps and institutional affiliations.